INSTITUT DE FRANCE
Académie des sciences

Comptes Rendus

Physique

Jianju Tang, Hongyi Yu, Chih-Kang Shih and Wang Yao

Moiré excitons at line defects in transition metal dichalcogenides heterobilayers

Volume 22, Special Issue S4 (2021), p. 53-68

Published online: 1 March 2021
Issue date: 8 March 2022

https://doi.org/10.5802/crphys.50

Part of Special Issue: Recent advances in 2D material physics
Guest editors: Xavier Marie (INSA Toulouse, Université Toulouse III Paul Sabatier, CNRS, France) and Johann Coraux (Institut Néel, Université Grenoble Alpes, CNRS, France)

Les Comptes Rendus. Physique *sont membres du Centre Mersenne pour l'édition scientifique ouverte*
www.centre-mersenne.org
e-ISSN : 1878-1535

Comptes Rendus
Physique
2021, 22, nº S4, p. 53-68
https://doi.org/10.5802/crphys.50

Recent advances in 2D material physics / *Physique des matériaux bidimensionnels*

Moiré excitons at line defects in transition metal dichalcogenides heterobilayers

Excitons de moiré au niveau des défauts de ligne dans les hétérocouches de dichalcogénures de métaux de transition

Jianju Tang [a, b], Hongyi Yu [a, c], Chih-Kang Shih [d] and Wang Yao* [a, b]

[a] Department of Physics, the University of Hong Kong, Hong Kong, China

[b] HKU-UCAS Joint Institute of Theoretical and Computational Physics at Hong Kong, China

[c] Guangdong Provincial Key Laboratory of Quantum Metrology and Sensing, and School of Physics and Astronomy, Sun Yat-Sen University (Zhuhai Campus), Zhuhai 519082, China

[d] Department of Physics, University of Texas at Austin, Austin, TX 78712, USA

E-mails: u3004113@connect.hku.hk (J. Tang), yuhy33@mail.sysu.edu.cn (H. Yu), shih@physics.utexas.edu (C.-K. Shih), wangyao@hku.hk (W. Yao)

Abstract. In heterobilayers of 2D semiconductors, moiré pattern forms due to the inevitable lattice mismatch and twisting. Earlier works have shown that interlayer excitons in long-period moiré pattern experience a pronounced superlattice potential and have nanoscale patterned light-coupling properties. This leads to remarkable new possibilities to explore exciton physics and tailor optical properties. Line defects such as twin domain boundaries are commonly found in semiconducting transition metal dichalcogenides monolayer, which, in the context of a heterobilayer, leads to an interface between the R-stacking moiré and H-stacking moiré. Here, we show that such interface created by twin-domain boundary realizes a line-defect in the moiré superlattices for interlayer excitons, which localises a one-dimensional exciton mode of topological origin. The defect configuration in the moiré exciton superlattices can be continuously tuned by the interlayer translation and twisting angle, and is also a reflection of the atomic configuration of the domain boundary. The dispersion, wavefunction, and light coupling properties of the interface exciton modes are investigated at different superlattice defect configurations.

Keywords. moiré exciton, 2D semiconductors, Twin boundary, Van der Waals heterostructure, moiré superlattices.

Available online 1st March 2021

* Corresponding author.

1. Introduction

Semiconducting transition metal dichalcogenides (TMDs) monolayers feature direct band gap in the visible frequency range, exotic valley physics, strong spin–orbit coupling, and exceptionally strong Coulomb interaction, which have attracted great interest for exploring semiconductor optics and device applications in the atomically thin limit [1–5]. These monolayers have degenerate band edges located at the Brillouin zone corner $\pm K$, labeled by the valley pseudospin, which is an effective quantum degree of freedom of carriers that can be addressed by electrical and optical controls [6–11]. Exciton formed by Coulomb binding of an electron–hole pair inherit the valley optical selection rule of the band edges [12, 13], through which an exciton at $K(-K)$ valley can be interconverted with a $\sigma_+(\sigma_-)$ photon. Monolayer excitons, on the other hand, have short radiative lifetime and fast valley depolarization [14–16], which have limited their uses for practical valley-functional devices. Heterobaliyers of TMDs provide a way to overcome these limitations [17–20]. Their type-II band alignment leads to the layer separation of the electron and hole components in the exciton [20]. While retaining the valley optical selection rule [21], the recombination lifetime and the valley depolarization time are substantially increased because of the quench of the electron hole wavefunction overlap in the interlayer configuration [22]. Such interlayer excitons have attracted remarkable interest for the exploration of valleytronic and optoelectronic applications based on TMDs heterostructures [23–30].

In heterobilayers, small lattice mismatch and twisting between the TMDs building blocks will lead to the formation of a long-period moiré pattern, i.e. periodic spatial variation in interlayer atomic registries, which has intriguing effects on the interlayer excitons [21, 31]. With the sensitive dependence of interlayer coupling and optical transitions on the atomic registries [21, 32], the moiré pattern realizes a pronounced periodic potential landscape for interlayer exciton [33], as well as the nanoscale patterning of its light-coupling properties [31, 34, 35]. Consequently, the moiré excitons can be confined in an array of quantum dot like potential traps with circularly polarised valley optical selection rules. In relative small moiré, lateral hopping of excitons between the traps further leads to an excitonic superlattice with in situ strong spin–orbit coupling [31]. Possible experimental signatures of such moiré excitons are recently reported [23–25].

Twin boundaries are line defects that are commonly found in monolayer TMDs grown by CVD and MBE [36–46]. In the heterobilayers, the existence of twin boundaries in one layer introduces a one-dimensional interface between regions of H-stacking and R-stacking respectively. Theoretical calculations have shown that interlayer excitons experience distinct spin-valley optical selection rules and potential landscapes in the moiré formed in H-type and R-type heterobilayers [31, 34]. The properties of moiré excitons at such interface between the H-type and R-type heterobilayers realized by the twin boundary are intriguing to explore, with practical relevances.

Here we show that the twin boundary in a monolayer building block of the heterobilayer corresponds to a line defect in the moiré superlattice for interlayer excitons, interfacing the R-type and H-type moirés of distinct landscape and optical selection rules. The orientation and configuration of the superlattice line defect are sensitively controlled by the twisting angle and interlayer translation between the two monolayers, as well as atomic configuration of the twin boundary. A one-dimensional exiton mode of topological origin can be localized at such line defect, which features unusual dispersion relation and light coupling properties. Within the light cone where the exciton can be directly interconverted with photon, the defect exciton mode realizes a helical channel inside the gap of the excitonic minibands, where the velocity and detuning from the miniband edge can be tuned by interlayer bias. Remarkably, we find that the defect exciton mode can also provide information on the transmission of band edge carriers through the twin boundary. The dispersion of the exciton mode is dependent on the amplitude of transmission. The optical transition dipole of the exciton mode has both in-plane and out-of-

plane components. The ratio of the in-plane and out-of-plane dipole, as well as the polarization angle of the in-plane dipole, provide a sensitive probe on the phase of carrier transmission across the twin boundary.

The rest of the paper is organized as follows. Section 2 presents the dependence of geometric configuration of the moiré superlattice line defect on the twin-boundary atomic configuration, and twisting angle and interlayer translation between the two layers. In Section 3, we analyse the hopping of low energy interlayer excitons between the moiré trapping sites across the line defect. A tight-binding model describing the interface of the R-type and H-type moiré exciton superlattice is constructed with up to the third nearest neighbor hopping. In Sections 4 and 5, we focus on the example of zigzag moiré line defect in zero twisting heterobilayer. The dispersion of the defect exciton mode is analyzed in Section 4, under different atomic configurations and transmission amplitudes of band edge carrier through the twin-boundary. In Section 5, we investigate the optical transition dipole of the moiré exciton interface mode and its dependence on the phase of carrier transmission amplitude across the twin boundary.

2. Geometric configurations of the superlattice line defect

Figure 1(a) schematically shows a heterobilayer with top and bottom gates. There is a zigzag twin-boundary in the top layer, so to the left side of the twin boundary, the R-stacking heterobilayer is formed, while to the right side, the heterobilayer is H-stacked. The figure also illustrates a split double gate design with the twin-boundary lying in the gap, which allows most control flexibility with separate interlayer bias control of the R- and H-stacking regions. But as we will discuss later, a global top and bottom gating may also be sufficient.

The lattice mismatch and rotation misalignment between the individual layer of the heterobilayer lead to moiré patterns in these two regions with distinct stacking orders. Due to the same lattice constants and relative twist angle in these two regions caused by rotating the bottom layer, both moiré patterns in the R-stacking region and H-stacking region have the same periods and superlattice orientations. In the moiré pattern, we trace the three high symmetry locals A, B, C, where the local atomic stackings retain the C_3 rotational symmetry. The interlayer stacking registries at these three locals are respectivley R_h^h, R_h^X, R_h^M (H_h^X, H_h^h, H_h^M) in R-stacking (H-stacking) region, as shown in Figure 1(b, c). Earlier works have shown that in the R-stacking moiré, A and B points are energy minima that trap moiré excitons, and C points are the energy maxima, whereas in the H-stacking region, A and C points are the energy minima, and B points are the energy maxima [31]. These energy landscapes then define honeycomb superlattices in the R- and H-stacking regions respectively.

Clearly there can be a mismatch at the interface between the R- and H-stacking moiré, which forms a line defect in the whole superlattice (see Figure 1(c)). The moiré line defect configuration is controlled by interlayer twist angle θ, interlayer translation $\delta\boldsymbol{l}$ and the width of twin boundary $|\boldsymbol{d}|$. Here $\boldsymbol{d}$ is the vector connecting two metal atoms from the left side zigzag edge to the right side zigzag edge in the twin-boundary (see Figures 1(a) and 3(c)). In the following, we first discuss how the line defect configuration in the moiré superlattice changes with the control parameters.

We choose the coordinate frame that the twin-boundary in the top layer is along the y direction (the bottom layer will be rotated with the small twist angle θ). The moiré superlattice period in the R-tacking region and H-stacking region can be uniformly expressed in term of the twist angle θ and lattice mismatch ε as [47]

$$b \equiv \left|\boldsymbol{L}_i^M\right| = \left|\boldsymbol{R}_i^M\right| = \frac{1+\varepsilon}{\sqrt{\varepsilon^2 + 2(1+\varepsilon)(1-\cos\theta)}}\, a. \tag{1}$$

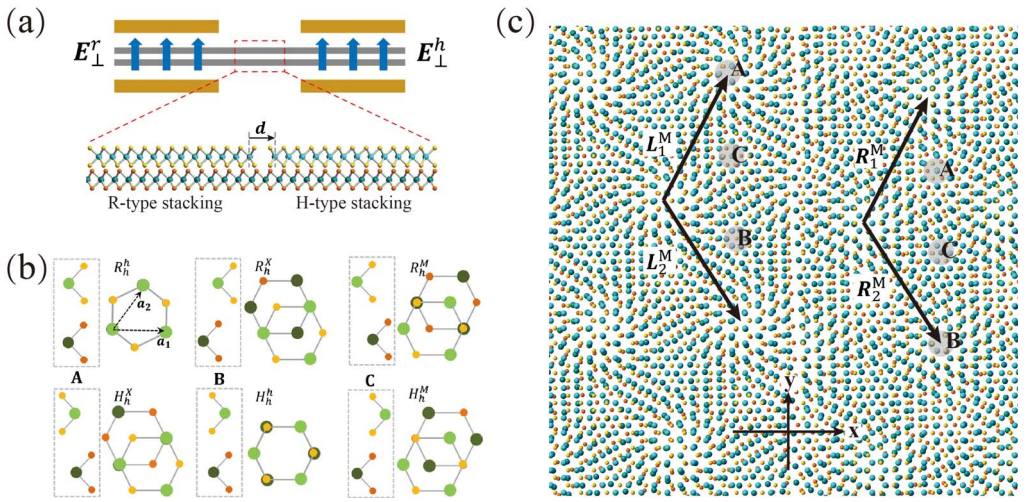

Figure 1. (a) The heterobilayer is set up in the splitting gate. The system with R type stacking in the leftside and H-type stacking in the rightside. The electric field along the z direction can be different in R-stacking and H-stacking regions, denoted by $\boldsymbol{E}_\perp^r$, $\boldsymbol{E}_\perp^h$. (b) The local stacking configuration of A, B, C, points, where $R_h^\mu(H_h^\mu)$ denotes a R-type (H-type) stacking with μ-site of upper layer coincided with hexagon center(h) of lower layer. (c) moiré superlattices are shown in the R-stacking and H-satcking regions with their primitive vectors $\boldsymbol{L}_i^M$ and $\boldsymbol{R}_i^M$. The shaded A, B, C points are high symmetry points with C_3 symmetry. The primitive vectors of monolayer TMDs are $\boldsymbol{a}_1 = a\,(0\,,1)$, $\boldsymbol{a}_2 = a\,(\sqrt{3}/2, 1/2)$ with the lattice period a. The metal atoms and chalcogen atoms are denoted by cyan (green) spheres and yellow (orange) spheres in MoX_2 (WX_2), respectively.

where $\boldsymbol{L}_i^M$ and $\boldsymbol{R}_i^M$ denote the primitive vectors of the superlattice in the R-stacking and H-stacking regions respectively (Figure 1(c)). Use φ to denote the angle between the superlattice zigzag axis with the interface of R- and H-stacking regions (y coordinate axis), one find

$$\varphi = \arctan\left(\frac{\sin\theta}{1+\varepsilon-\cos\theta}\right), \tag{2}$$

in both the R-stacking and H-stacking region. The twist angle θ and lattice mismatch ε together control the orientation of the line-defect in the moiré superlattice, i.e. whether it is a zigzag, armchair, or a chiral one, although the underlaying twin-boundary is fixed to be zigzag. For example, in the $MoSe_2/WSe_2$ bilayer with $\varepsilon = 0.1\%$, one find $\varphi \approx 1.55$ at twist angle $\theta = 5°$, which means the superlattice line-defect is a chiral one. At small twist angle limit, one can get that $\varphi \approx \arctan(\theta/\varepsilon)$. A zigzag moiré line defect is formed at zero twist angle. In the limit that ε is negligible, $\varphi = (\pi - \theta)/2$.

With the line-defect orientation determined by θ and ε, its configuration can be further controlled by interlayer translation $\delta\boldsymbol{l}$, and is also a sensitive reflection of the twin-boundary parameter $\boldsymbol{d}$. It is easy to see that the interlayer translation (the translation of bottom layer by $\delta\boldsymbol{l}$, in the reference adopted here) will cause a common translation $\delta\boldsymbol{r}$ of the moiré superlattice sites in the R-stacking and H-stacking regions (see Figure 2(a)),

$$\delta\boldsymbol{r} = -\left(1 - M^{-1}\hat{R}^{-1}\right)^{-1} M^{-1}\hat{R}^{-1}\delta\boldsymbol{l} \tag{3}$$

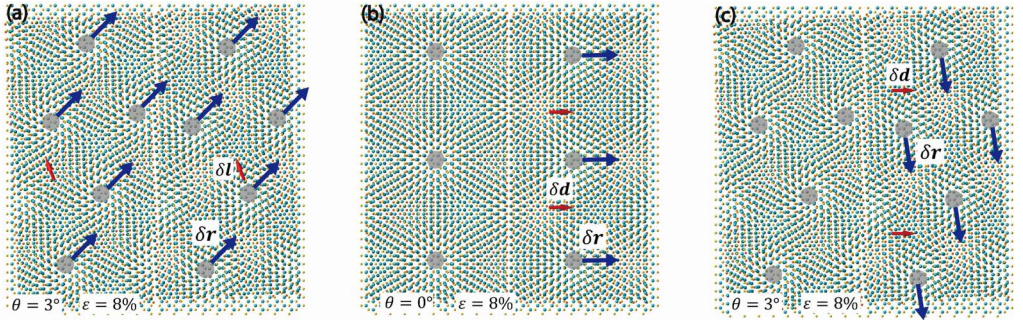

Figure 2. Schematic of the evolution of the moiré line defect configuration with the change of parameters. (We have enlarge the lattice match 8 times than that in $MoSe_2/WSe_2$ so that the moiré pattern can be shown in a small region.) (a) A relative translation $\delta\boldsymbol{l}$ (red arrows) of bottom layer causes a shift $\delta\boldsymbol{r}$ (darker blue arrows) of moiré superlattice sites common in both R-stacking and H-stacking regions. Both the twist angle θ and lattice mismatch ε are nonzero here. The shaded disks denote the A (B) sites in the R-stacking (H-stacking) region. (b) At zero twisting, the variation $\delta\boldsymbol{d}$ in the twin-boundary width produces a translation of moiré superlattice sites in the H-stacking in the x direction, which changes the superlattice line-defect width. (c) At non-zero twist angle θ, $\delta\boldsymbol{r}$ can have both x and y components. When θ is much large compared to the lattice mismatch ε, the same $\delta\boldsymbol{d}$ cause a translation $\delta\boldsymbol{r}$ of moiré superlattice sites nearly along y direction. The width of the superlattice line-defect is unchanged, but the sites registry between its two sides are changed.

where $M = 1+\varepsilon$, and $\hat{R} \equiv \hat{R}(\theta)$ is the operator describing in-plane anti-clockwise rotation. For the example of zero twist angle $\theta = 0$, $\delta\boldsymbol{r} = -(1/\varepsilon)\delta\boldsymbol{l}$, where a tiny interlayer translation $\delta\boldsymbol{l}$ will cause a magnified shift (by a sizeable factor of ε^{-1}) of the moiré superlattice along the same direction.

The parameter $\boldsymbol{d}$ controls the relative displacement between the superlattice sites of the R-stacking and H-stacking region. We illustrate below how the superlattice configuration evolves when the value of $\boldsymbol{d}$ is varied, which can always be decomposed as a translation of half of the upper layer by $\delta\boldsymbol{d}$, plus an overall interlayer translation $\delta\boldsymbol{l}$. The role of the latter has been analyzed above. And we find that $\delta\boldsymbol{d}$ simply causes a shift $\delta\boldsymbol{r}$ in the superlattice sites at the corresponding half of the moiré (Figure 2(b–c)),

$$\delta\boldsymbol{r} = \left(1 - M^{-1}\hat{R}^{-1}\right)^{-1}\delta\boldsymbol{d}. \tag{4}$$

By definition, $\boldsymbol{d}$ is along x direction (Figure 1(a)), so its variation $\delta\boldsymbol{d} = (\delta d, 0)$. At zero twisting, we find

$$\delta\boldsymbol{r} = \left(\delta r_x, \delta r_y\right) = \delta d\left(\frac{1+\varepsilon}{\varepsilon}, 0\right), \tag{5}$$

i.e. the value of $\boldsymbol{d}$ controls the relative displacement in the x direction between the R-stacking and H-stacking moiré sites (see Figure 2(b)). In other words, it controls the width of moiré line defect. At finite twist angle, we have

$$\delta\boldsymbol{r} \approx \delta d\left(\frac{1+\varepsilon}{\varepsilon}, -\frac{1+\varepsilon}{\varepsilon^2}\theta\right). \tag{6}$$

The displacement $\delta\boldsymbol{r}$ of the superlattice sites in the corresponding stacking region has both x- and y-components, see Figure 2(c). For $\varepsilon \ll \theta$, $\delta\boldsymbol{r}$ would be nearly perpendicular to $\delta\boldsymbol{d}$. The width of the superlattice line-defect is unchanged, but the sites registry between its two sides are changed.

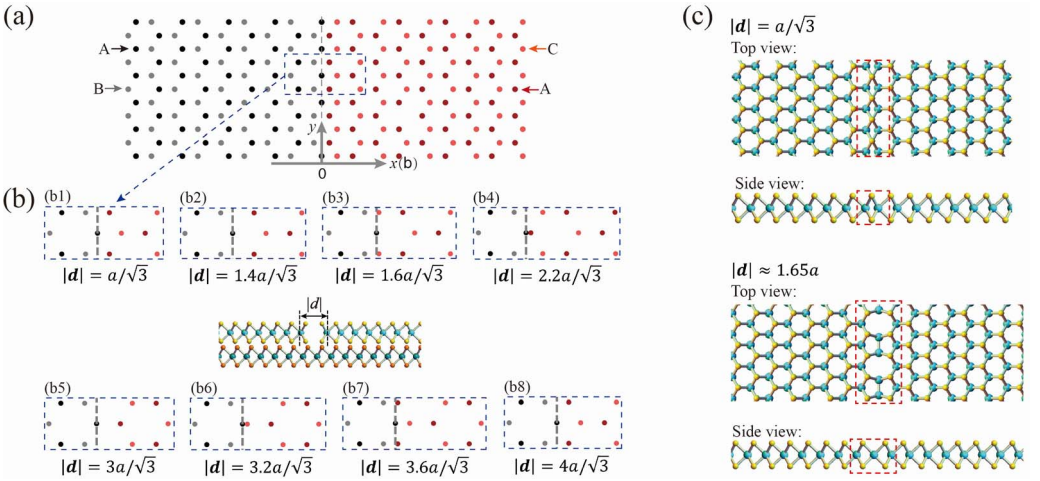

Figure 3. (a, b) Line-defect configurations in the moiré superlattice, under various width $|\boldsymbol{d}|$ of the twin-boundary. The black dots and gray dots denote, A and B in the R-stacking region, respectivley. While the darker red and lighter red are A and C points in the H-stacking region. The gray dashed line denotes the zigzag edge of R-stacking region of moiré superlattice. Eight configurations of the moiré line defect are shown under various values of $|\boldsymbol{d}|$, where a is the lattice constant of monolayer TMDs. (c) Two twin boundary configurations from [41].

Figure 3 gives a more detailed account of the superlattice line defect configurations at the various d values, for the example of $MoSe_2/WSe_2$ heterobilayer ($\varepsilon = 0.1\%$), at $\theta = 0$. The line defect is along the zigzag direction. When $|\boldsymbol{d}|$ increases from $a/\sqrt{3}$ to $4a/\sqrt{3}$, a whole column of superlattice hexagon emerges, shifting the superlattice sites to the right of the line defect by $\sqrt{3}b$. In Figure 3(c), two different twin boundary configurations determined in experiments are shown for reference.

As a brief summary of this part, various line-defect configurations (orientation, width and site registry) can be realized in the heterobilayer moiré superlattice, controlled by the lattice mismatch, twisting, interlayer translation, and twin-boundary width. This points to rich possibilities to engineer interface mode of moiré excitons. Such mode can be of topological nature, as we will show below using the example of the zero twist angle heterobilayer. We choose the line-defect in (b1) and (b5) of Figure 3 as the representative configurations as demonstration. In previous studies [37, 38, 41–46], the widths of observed twin boundaries are about $0.8a$, $1.1a$, or $1.65a$ with the lattice constant a, in the atomic scale. While the induced moiré line defect should have widths in the order of moiré-period and been controlled by $|\boldsymbol{d}|$ in the zero twisted angle cases.

3. Hopping of interlayer excitons between the moiré trapping sites

The MoX_2/WX_2 heterobilayers have conduction band edge and valence band edge located in different layers, i.e. a type-II band alignment, in which interlayer excitons are energetically favorable with electrons in the MoX_2 (upper) layer and holes in the WX_2 (bottom) layer. Since the electron and hole constituents are separated in different layer, the interlayer exciton has an electric dipole. In the moiré pattern, the periodic variation of interlayer atomic registry results in periodically modulated local bandgap E_g and interlayer distance d. Thus, the interlayer exciton in the moiré pattern would experience a superlattice potential with same period of moiré

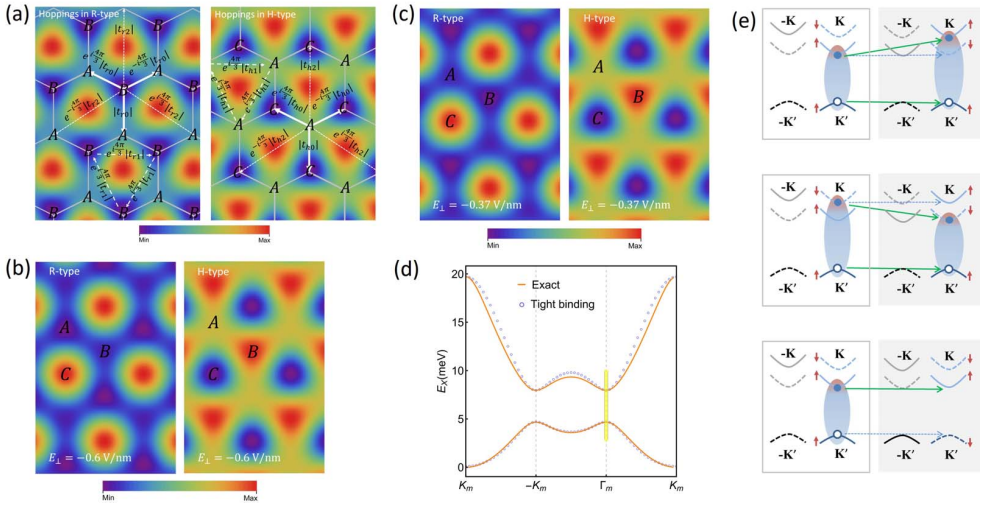

Figure 4. (a) The moiré potential in the R-type and the H-type $MoSe_2/WSe_2$ heterobilayer at $E_\perp \approx 0$ V/nm. The complex hopping phase for up to third nearest neighbor hopping are shown. (b–c) The moiré potentials in the R-type and H-type region with applied different external electric field. (d) The lowest two mini-bands for spin up excitons in the R-stacking region, calculated exactly from the moiré potential (c), and calculated with the tight binding model with up to third nearest neighbor hopping. (e) Schematic of the hopping of interlayer exciton across the line-defect. The zigzag oriented twin-boundary conserves the valley index. With the twin-boundary lying in the electron layer (upper two panels), the electron band edge has opposite spin splitting in the R-stacking and H-stacking regions. The bottom panel illustrates the different situation where the twin-boundary lies in the hole layer, where hole has to flip spin for the exciton to hop across the line defect. Solid (dashed) curves denote spin up (down) band edges. Solid (dotted) arrows denote spin conserved (flipped) hopping of electron or hole.

superlattice [31]. Through exciton's electric dipole, such moiré potential can be tuned by an perpendicular electric field $E_\perp$. The superlattice potential for the interlayer exciton is then,

$$V(\boldsymbol{R}) = E_g(\boldsymbol{R}) + eE_\perp d(\boldsymbol{R}) - E_b, \tag{7}$$

where $\boldsymbol{R}$ is the location in the moiré, and E_b denotes exciton binding energy. For the example of $MoSe_2/WSe_2$ heterobilayer, the potential landscape $V(\boldsymbol{R})$ at a given electric field is shown as the color maps in Figure 4(a–c), plotted using the formula and parameters extracted from first principle band structure calculations given in [31].

The moiré potential extrema appear at the mentioned high symmetry locals, A, B, C due to the constraint of C_3 symmetry. Note that the A, B (A, C) points are the local potential minima in the R-stacking (H-stacking) region, which are trapping sites of the interlayer excitons, while the C (B) points are potential maxima in R-stacking (H-stacking) region of moiré pattern. The excitons at those high symmetry points have valley optical selection rules determined by the local atomic registry [31,34]. When the moiré period is relatively small, the trapped excitons have lateral hopping between the trapping sites, forming an excitonic honeycomb superlattice.

Unlike other realization of superlattice potential, the hopping matrix element of the interlayer exciton in the moiré superlattice uniquely carries a complex phase,

$$t_\beta(\boldsymbol{R}_1 - \boldsymbol{R}_2) = \mathrm{e}^{\mathrm{i}(\boldsymbol{K}-\boldsymbol{K}')\cdot(\boldsymbol{R}_1-\boldsymbol{R}_2)} \left| t_\beta(\boldsymbol{R}_1 - \boldsymbol{R}_2) \right|, \tag{8}$$

where $\boldsymbol{R}_1$ and $\boldsymbol{R}_2$ are the initial and final sites, and $\boldsymbol{K}(\boldsymbol{K}')$ is the electron (hole) valley center. The hopping amplitude t_β depends on the potential landscape and can be different in the R-stacking ($\beta = r$) and H-stacking ($\beta = h$) moiré, while the phase does not and has the same form in the R-stacking and H-stacking regions.

We note that this complex hopping phase introduces the spin dependence [31]. In monolayer TMDs, the valence band edge is spin-valley locked [8], namely, one find spin down (up) hole only at valley $\boldsymbol{K}'$ ($-\boldsymbol{K}'$), as shown in Figure 4(e). Consequently, interlayer exciton also has its spin index locked to the valley index. As shown in Figure 4(e), at a given electron–hole valley configuration $(\boldsymbol{K}, \boldsymbol{K}')$, spin-triplet and spin-singlet exciton species have different energies due to the conduction band spin splitting. If we concern about one of these species, e.g. the spin-singlet exciton, its two degenerate configurations, the spin up and down excitons have the valley configurations $(\boldsymbol{K}, \boldsymbol{K}')$ and $(-\boldsymbol{K}, -\boldsymbol{K}')$ respectively. The hopping terms for spin up excitons are given in (8), while the hopping terms for the spin down excitons is the time reversal counterpart at $(-\boldsymbol{K}, -\boldsymbol{K}')$, i.e. the complex conjugate of (8). Such spin-dependence in the complex hopping phase introduces sizable spin–orbit splitting in the exciton mini-bands [31].

The low energy excitons in such honeycomb superlattice can be described by a two-orbital tight binding model (Figure 4) [31]. Figure 4(d) shows a comparison of the lowest two exciton mini-bands in the R-stacking region calculated exactly from the moiré potential $V(\boldsymbol{R})$ in Figure 4(c), and that from the tight binding model with up to third nearest neighbor hopping, at a moiré period $b = 10$ nm. The parameters used in the tight-binding model are $t_0 = 3.07$ meV for the magnitude of first nearest neighbor hopping, $t_1 = 0.40$ meV for second nearest neighbor hopping, $t_2 = 0.15$ meV for third nearest neighbor hopping, and energy difference $m = -0.53\,t_0$ between the A and B sites. Figure 4(d) shows only the mini-bands of spin up excitons, which feature two Dirac cones at the Γ_m and $-K_m$ points of the mini Brillouin zone. These Dirac cone locations are clearly distinct from a typical honeycomb lattice, which are displaced by the wavevector $\boldsymbol{K}_m \equiv \boldsymbol{K} - \boldsymbol{K}'$ that lies in the complex hopping phases in (8). The spin down excitons' mini-bands are obtained as their time reversal.

Now we turn to the near neighbor hopping of exciton between the moiré superlattice sites on the two sides of the line defect. The hopping of the hole component conserves both spin and valley indices, as hole layer is a continuous lattice through the two regions. With the twin-boundary lying in the electron layer, the complex electronic structure at the low-symmetry twin-boundary may lead to both spin-conserved and spin-flipped hopping of the electron. So in general, hopping matrix element is allowed between a spin singlet exciton in R-region with both spin singlet and spin triplet exciton at the same valley in H-region. If the twin-boundary lies in the hole layer, then hole has to flip spin for the exciton to hop across the line defect (see Figure 4(e)).

The width of twin boundary is orders smaller than that of the moiré line defect. When the interlayer exciton hops across the moiré line defect, the role of the twin boundary at a distance much larger than d can be described as an extra phase shift $\mathrm{e}^{\mathrm{i}\phi}$ and a change in the magnitude of the hopping matrix element, on top of the form described by (8)),

$$t_{rh} \equiv \mathrm{e}^{\mathrm{i}\phi}\alpha\, t_r, \tag{9}$$

where t_r is the hopping matrix element in the pristine moiré superlattice. ϕ is a constant here, corresponding to the phase shift in the transmission coefficient of the one-dimensional scattering of electron by the twin-boundary. The factor α accounts for both the amplitude of this transmission coefficient, as well as the effect of the different energy landscape $V(\boldsymbol{R})$ at the line-defect seen by the moiré exciton. Their values are subject to the details of the twin-boundary and moiré line-defect configurations, and we will show below that α will manifest in the dispersion

of the moiré exciton interface mode. The phase shift ϕ has no effect on the dispersion, but will manifest in the optical transition dipole of the interface mode.

We note that moiré excitons in the R-type and H-type heterobilayers in general can have an energy offset Δ_{rh}, which are measured to be in the order of a few tens of meV in $MoSe_2/WSe_2$ heterobilayers [23]. Δ_{rh} significantly larger than the nearest neighbor hopping amplitude t_0 can decouple the R-stacking and H-stacking moiré superlattice, giving rise to two separate edge modes at the line-defect. Δ_{rh} could be contributed by the conduction band splitting (Figure 4(e)), and the binding energy difference due to the slightly different interlayer distances in R- and H-stacking. The latter can be used to tune Δ_{rh} in a uniform perpendicular electric field. Besides, the split double-gating shown in Figure 1(a) allows applying different electric field to the R-stacking and H-stacking regions. These control possibilities allow tuning Δ_{rh} to small value so that interlayer exciton can efficiently hop across the line-defect, the effect of which we explore below. We focus on hopping between the same spin species on both sides, e.g. spin singlet, in which case the spin-flipped hopping, i.e. between singlet and triplet, will be suppressed by their energy offset. Alternatively, spin singlet in the R-stacking region can also be tuned into near resonance with the spin triplet in the H-stacking region (or vice versa) to allow their spin-flipped hopping, whereas other exciton species become irrelevant.

4. Dispersion of the moiré exciton interface mode

The dispersions of the moiré exciton interface mode can be classified into several types determined by the sign of the site energy difference $m_r = V(\boldsymbol{R}_B) - V(\boldsymbol{R}_A)$ in the R-stacking region, that in the H-stacking region $m_h = V(\boldsymbol{R}_A) - V(\boldsymbol{R}_C)$, and the energy offset Δ_{rh} between the two regions. As discussed earlier, the bulk mini-band dispersion is reminiscent of that of graphene, expect for the displacement of the Dirac cones by the wavevector $\boldsymbol{K}_m \equiv \boldsymbol{K} - \boldsymbol{K}'$. m_β corresponds to the Dirac mass, which opens a gap. The gapped Dirac cone features a half-quantized topological charge, with sign determined by the sign of m_β. If the mass has opposite sign in the honeycomb lattice on the two sides of the interface, the quantized change of the bulk topological charge across the interface dictates a chiral channel inside the gap of each cone [48]. Figure 5(a) shows the exciton mini-bands dispersion corresponding to such a case. The blue and red color denote respectively the spin up and down excitons. For each spin, there is a in-gap chiral channel at the Dirac cones at the mini-Brillouin zone center and corner. Only the zero momentum excitons in a small neighborhood of the mini-BZ center, referred as the light cone ($k_c \approx 0.01$/nm), can satisfy the momentum conservation for coupling to photon. Within the light cone, the interface moiré exciton mode realizes a one-dimensional spin helical channel.

Figure 5(b) shows a different type of moiré exciton dispersion, where the sign of mass m_r is the same as m_h. In such case, the interface mode becomes a rather flat 1D band, connecting the Dirac cones at the mini-BZ center and corner. The dispersion shown is for the spin up exciton, while the spin down one can be obtained as its time reversal. The relative sign the Dirac masses m_r and m_h can be tuned by the perpendicular electric field, making use of the location dependent exciton electric dipole $ed(\boldsymbol{R})$ in the moiré (cf. (7)). Figure 4(b–c) show two examples of the moiré potentials $V(\boldsymbol{R})$ in the R-stacking and H-stacking regions. The mass m_r in the R-stacking regions is reversed when the electric field value changes from $E_\perp = -0.37$ V/nm to -0.6 V/nm, while the sign of m_h is unchanged.

Figure 5(c) shows yet another type of interface mode dispersion, in the case of very large Δ_{lr}, which effectively decouples the low energy exciton mini-band in the R-stacking region from that in the H-stacking region, leading to the flat-band edge states like those observed at the zigzag edges of graphene [48]. We note that our tight-binding model constructed with the ground state in each moiré trapping site only accounts the lowest two exciton mini-bands in either sides. There

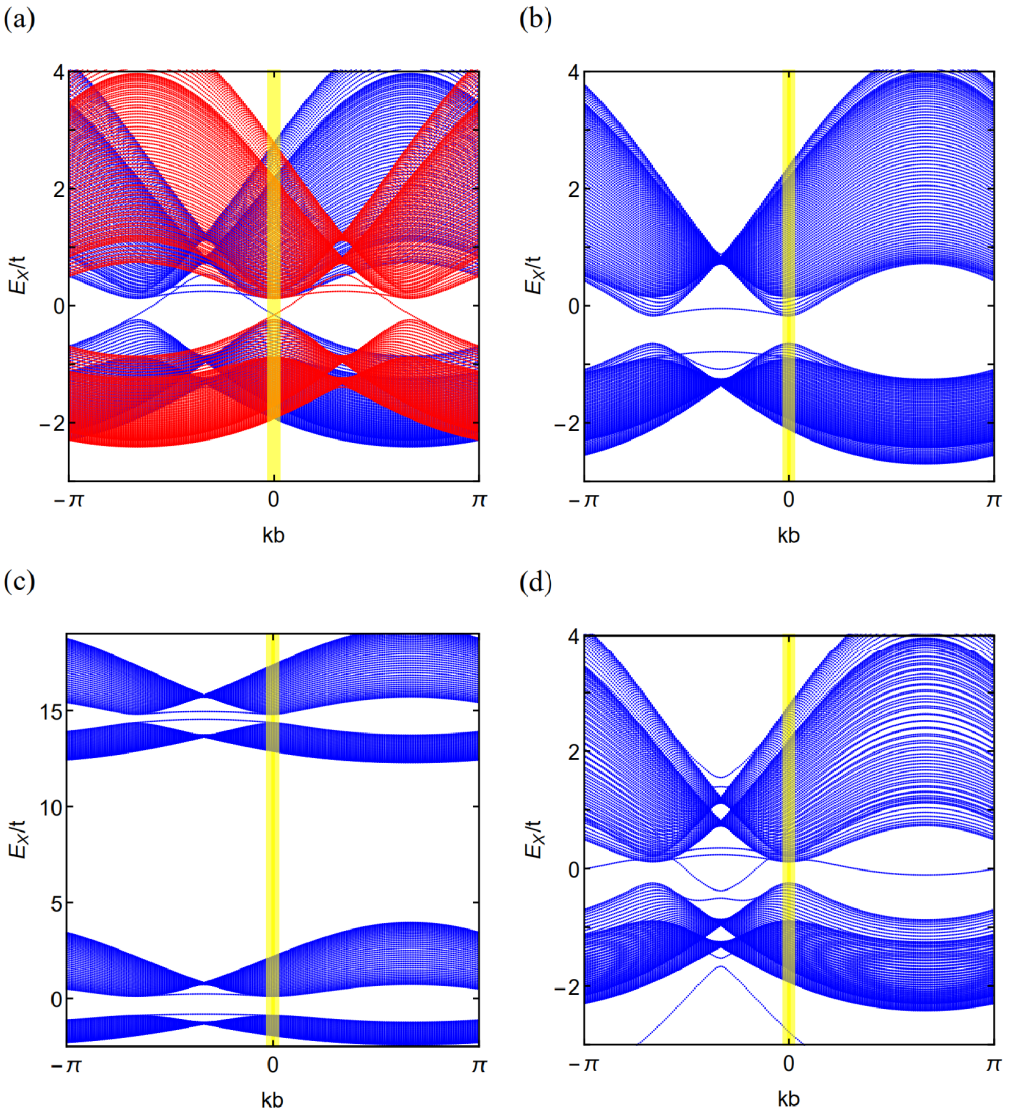

Figure 5. (a) The mass of exciton tight binding model in R-stacking region ($m_r = -0.5t$) is larger than that in the H-stacking region ($m_h = 0.2t$). The spin up (blue) and down (red curve) exciton dispersions are shown with helical edge states in the light cone highlighted in yellow color. (b) The sign of the mass of exciton tight binding in R-stacking region ($m_r = 0.5t$) is the same as that in the H-stacking region ($m_h = 0.2t$). There are two flat bands at the moiré line defect connecting the Dirac points. (c) The large energy difference ($\Delta_{rh} = 15t$) effectively decouples excitons in the R-stacking region (with $m_r = -0.5t$) from that in the H-stacking region ($m_h = 0.2t$). (a–c) Corresponds to the same line defect configuration (b5). (d) The dispersion of moiré excitons with $m_r = -0.5t$, $m_h = 0.2t$ for line defect configuration (b1). For (a–d), detail values of parameters used in the tight binding model are listed in Table 1. For $b = 10$ nm moiré size, the light cone size has width $2k_c b \approx 0.2$ around the origin. The energy unit here $t = 3.07$ meV.

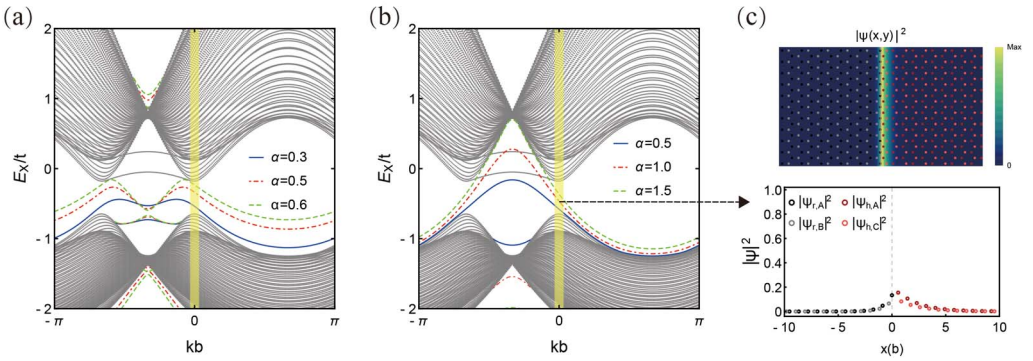

Figure 6. (a) The dependence of interface mode dispersion on α, the magnitude of the hopping across the line defect (cf. (9) in the text). The defect configuration considered is (b1) in Figure 3. (b) Exciton interface mode dispersion at line defect configuration (b5), at the different α values. (c) An example of the wave function of the interface state in the light cone, with $\alpha = 1.0t$. For (a–c), the detailed values of parameters in the tight binding model are listed in Table 3.

Table 1. Values of parameters in each sub-figure of Figure 5 in the tight binding model, $t = 3.07$ meV

(a) With boundary config. (b5)		(b) With boundary config. (b5)	
$t_{r0} = -t,$	$t_{h0} = -1.12t$	$t_{r0} = -t,$	$t_{h0} = -1.12t$
$t_{r1} = 0.129t,$	$t_{h1} = 0.137t$	$t_{r1} = 0.129t,$	$t_{h1} = 0.137t$
$t_{r2} = -0.05t,$	$t_{h2} = -0.052t$	$t_{r2} = -0.05t,$	$t_{h2} = -0.052t$
$m_r = -0.5t,$	$m_h = 0.2t$	$m_r = 0.5t,$	$m_h = 0.2t$
$\Delta_{rh} = 0.4t,$	$\alpha = 1.0t$	$\Delta_{rh} = 0.0t,$	$\alpha = 1.0t$
(c) With boundary config. (b5)		(d) With boundary config. (b1)	
$t_{r0} = -t,$	$t_{h0} = -1.12t$	$t_{r0} = -t,$	$t_{h0} = -1.12t$
$t_{r1} = 0.129t,$	$t_{h1} = 0.137t$	$t_{r1} = 0.129t,$	$t_{h1} = 0.137t$
$t_{r2} = -0.05t,$	$t_{h2} = -0.052t$	$t_{r2} = -0.05t,$	$t_{h2} = -0.052t$
$m_r = -0.5t,$	$m_h = 0.2t$	$m_r = -0.5t,$	$m_h = 0.2t$
$\Delta_{rh} = 15t,$	$\alpha = 1.0t$	$\Delta_{rh} = 0.4t,$	$\alpha = 1.0t$

also exist higher energy mini-bands arising from excited states at the moiré trapping sites (i.e. with p- or d-wave envelope functions) [31, 35]. In the large Δ_{rh} limit, the higher energy mini-bands in the R-stacking region can overlap in energy with the mini-bands in H-stacking region, or vice versa, which can be coupled by exciton hopping across the line defects. These can also lead to interface exciton modes like those addressed in Figure 5(a,b).

The dispersions of the interface mode also depend strongly on configurations of the moiré line defect. Figure 5(d) shows the dispersions at line-defect configuration (b1) which is drastically different from those of configuration (b5) shown in Figure 5(a) under the same parameters. For the (b5) case, the superlattice sites still preserve the hexagonal lattice configurations, except that the onsite energies and near neighbor hopping have changed across the line defect. In contrast, for (b1), the sites at the line defects have been completely rearranged from hexagonal configuration, giving rise to more complex interface exciton modes.

Besides, the magnitude of hopping across the line defect, t_{rh}, also has impacts on the interface mode dispersion. The dispersions under line defect configuration (b1) and (b5) under different

Table 2. Nontrivial exciton edge state cases, $t = 3.07$ meV

Config. (b1), $\theta = 0$	Config. (b5), $\theta = 0$
$\lvert\boldsymbol{d}\rvert = a/\sqrt{3}$	$\lvert\boldsymbol{d}\rvert = 3a/\sqrt{3}$
$\mathrm{sgn}[m_r] = -\mathrm{sgn}[m_h]$	$\mathrm{sgn}[m_r] = -\mathrm{sgn}[m_h]$
$\alpha = 0.2 \sim 0.8t$	$\alpha = 0.5 \sim 1.8t$

Table 3. Values of parameters in each sub-figure of Figure 6 in the tight binding, $t = 3.07$ meV model

(a) With boundary config. (b1)		(b) With boundary config. (b5)		(c) With boundary config. (b5)	
$t_{r0} = -t,$	$t_{h0} = -1.12t$	$t_{r0} = -t,$	$t_{h0} = -1.12t$	$t_{r0} = -t,$	$t_{h0} = -1.12t$
$t_{r1} = 0.129t,$	$t_{h1} = 0.137t$	$t_{r1} = 0.129t,$	$t_{h1} = 0.137t$	$t_{r1} = 0.129t,$	$t_{h1} = 0.137t$
$t_{r2} = -0.05t,$	$t_{h2} = -0.052t$	$t_{r2} = -0.05t,$	$t_{h2} = -0.052t$	$t_{r2} = -0.05t,$	$t_{h2} = -0.052t$
$m_r = -0.5t,$	$m_h = 0.2t$	$m_r = -0.5t,$	$m_h = 0.2t$	$m_r = -0.5t,$	$m_h = 0.2t$
$\Delta_{rh} = 0,$	$\alpha = 0.3t, 0.5t, 0.6t$	$\Delta_{rh} = 0,$	$\alpha = 0.5t, 1.0t, 1.5t$	$\Delta_{rh} = 0,$	$\alpha = 1.0t$

Table 4. The emission polarization of the moiré exciton with valley configuration $\{\boldsymbol{K}, \boldsymbol{K}'\}$ at the high symmetry points in the R-stacking and H-stacking region [34]

	R_h^h (A)	R_h^X (B)	R_h^M (C)	H_h^X (A)	H_h^h (B)	H_h^M (C)
Spin singlet	σ_+	σ_-	z	σ_+	σ_-	z
Spin triplet	z	σ_+	σ_-	z	σ_+	σ_-

values of α (cf. (9)) are shown in Figure 6. A common trend observed in both cases is that with the increase of α, there is a branch of interface mode dispersion that is blue shifted inside the bulk mini-gap, and consequently, the velocity and energy of the in gap mode in the light cone can be tuned. Finally, we summarize two specific cases, in which nontrivial exciton edge states exist at the moiré line defect. The parameters are listed in the Table 2.

5. Optical transition dipole of the moiré exciton interface mode

In this section, we focus on optical properties of the interface moiré excitons. At each moiré trapping site, the optical transition dipole of the moiré exciton is exclusive determined by the local atomic registry [31] and the spin-valley configuration. We have list the emission polarization of the exciton with the $(\boldsymbol{K}, \boldsymbol{K}')$ electron–hole valley configuration at the high symmetry stacking in Table 4. The spin singlet excitons have distinct optical selection rules from that of spin triplet ones. And unlike the monolayer exciton in TMDs where the optical dipole is dominated by the in plane one, the interlayer excitons can couple to either the in-plane $\sigma_\pm$ circularly polarized light or the out-of-plane (z) linearly polarized light.

The moiré exciton interface mode localized by the line defect has its wavefunction extended over the trapping sites in both the R-stacking region and H-stacking regions. Figure 6(c) shows an example of the wavefunction of the interface mode in the light cone, distributed over the few column of trapping sites on both sides of the interface. The optical dipole of the interface mode is then determined by the interference of the optical dipoles on these trapping sites. Specially, the phase shift of the moiré exciton obtained after crossing the twin boundary can be manifested in the light coupling.

The wave function of the 1D interface mode can be generally written as

$$\left|\psi_k(y)\right\rangle = \mathrm{e}^{\mathrm{i}ky}\left(\sum_i c^r_{i,A}\left|\chi^r_{i,A}\right\rangle + \sum_i c^r_{i,B}\left|\chi^r_{i,B}\right\rangle + \mathrm{e}^{\mathrm{i}\phi}\sum_i c^h_{i,A}\left|\chi^h_{i,A}\right\rangle + \mathrm{e}^{\mathrm{i}\phi}\sum_i c^h_{i,C}\left|\chi^h_{i,C}\right\rangle\right) \tag{10}$$

where the sum is over the number of supercells containing A and B points in the R-stacking region or A and C points in the H-stacking region along the x direction. $\left|\chi^r_{i,A}\right\rangle$ is the exciton wavepacket state at A point of ith supercell in R-stacking region of moiré pattern [31]. ϕ is the phase shift of exciton hopping matrix element across the line-defect (cf. (9)), corresponding to the phase shift in the transmission coefficient of the one-dimensional scattering of electron by the twin-boundary. In the light cone, the wavevector $k = 0$.

Consider first the spin triplet exciton, the optical transition dipole of the interface exciton mode is given by,

$$\boldsymbol{D}_T = \left(A^r + A^h\right)\boldsymbol{e}_z + B^r\boldsymbol{e}_+ + C^h\boldsymbol{e}_-, \tag{11}$$

where

$$A^r = \left(\sum_i c^r_{i,A}\right)D^r_z \text{ and } A^h = \mathrm{e}^{\mathrm{i}\phi}\left(\sum_i c^h_{i,A}\right)D^h_z$$

are the contributions from the A sites in the R-stacking and H-stacking regions respectively, contributing the out-of-plane z polarized component.

$$B^r = \left(\sum_i c^r_{i,B}\right)D^r_+$$

is the contribution from the B sites in the R-stacking region, with the σ_+ polarized dipole.

$$C^h = \mathrm{e}^{\mathrm{i}\phi}\left(\sum_i c^h_{i,C}\right)D^h_-$$

is from the C sites in the H-stacking region, contributing the $\sigma-$ polarized dipole. D^β_γ with $\gamma = +, -, z$ and $\beta = r, h$ represent the magnitude of the σ_+, σ_-, z polarized optical transition dipole of interlayer excitons at the C_3 symmetrical sites in the R-stacking region and H-stacking region. In general, the interface mode's optical dipole can have all the three orthogonal components. The in-plane and out-of-plane polarized dipole can be separately analyzed by selecting the propagation direction of the photon. Remarkably, ϕ manifests as the relative phase between the σ_+ and σ_- polarized components, whose interference leads to an elliptically polarized in-plane dipole with the major axis determined by ϕ.

For the spin singlet exciton, the optical dipole of an interface mode in the light cone can also be expressed generally as,

$$\boldsymbol{D}_S = \left(A^r + A^h\right)\boldsymbol{e}_+ + B^r\boldsymbol{e}_- + C^h\boldsymbol{e}_z, \tag{12}$$

with

$$A^r = \left(\sum_i c^r_{i,A}\right)D^r_+, \quad A^h = \mathrm{e}^{\mathrm{i}\phi}\left(\sum_i c^h_{i,A}\right)D^h_+,$$
$$B^r = \left(\sum_i c^r_{i,B}\right)D^r_-, \quad C^h = \mathrm{e}^{\mathrm{i}\phi}\left(\sum_i c^h_{i,C}\right)D^h_z.$$

The phase shift ϕ also manifests in the overall in-plane optical dipole, but in a more complex way that affects both the major axis and the ellipticity of the polarization.

6. Conclusions

We have studied the line defect configurations in the moiré superlattice of TMDs heterobilayers, due to a twin boundary in one of the layers, and the properties of 1D moiré exciton interface mode localized by such line defect. We have shown that the twisting angle, lattice mismatch, and interlayer translation can be exploited to realize a varieties of line defect configurations in the zigzag, armchair, and general chiral direction in the honeycomb moiré superlattice, whereas the line defect configuration is also a sensitive reflection of the width of the atomic twin-boundary configuration. These can be exploited to engineer various interface moiré exciton modes. For zigzag oriented line defects, we give some quantitative examples of the interface mode dispersions, which can either be flat bands connecting the Dirac nodes in the bulk mini-bands of excitons, or in-gap helical states in the light cone. The determining factors on the interface mode dispersion can be the Dirac mass (site energy differences) on the two sides of the line-defect which can be tuned by perpendicular electric field, the geometric configurations of the superlattice line defects, and the magnitude of the exciton hopping across the line defect.

Acknowledgements

The work is supported by the Research Grants Council of Hong Kong (Grants No. HKU17312916 and No. C7036-17W), and the University of Hong Kong (Seed Funding for Strategic Interdisciplinary Research).

References

[1] B. Radisavljevic, A. Radenovic, J. Brivio, I. V. Giacometti, A. Kis, "Single-layer MoS_2 transistors", *Nat. Nanotechnol.* **6** (2011), p. 147-150.
[2] X. Xu, W. Yao, D. Xiao, T. F. Heinz, "Spin and pseudospins in layered transition metal dichalcogenides", *Nat. Phys.* **10** (2014), p. 343-350.
[3] K. F. Mak, C. Lee, J. Hone, J. Shan, T. F. Heinz, "Atomically thin MoS_2: a new direct-gap semiconductor", *Phys. Rev. Lett.* **105** (2010), article no. 136805.
[4] A. Splendiani, L. Sun, Y. Zhang, T. Li, J. Kim, C.-Y. Chim, G. Galli, F. Wang, "Emerging photoluminescence in monolayer MoS_2", *Nano Lett.* **10** (2010), no. 4, p. 1271-1275.
[5] Q. H. Wang, K. Kalantar-Zadeh, A. Kis, J. N. Coleman, M. S. Strano, "Electronics and optoelectronics of two-dimensional transition metal dichalcogenides", *Nat. Nanotechnol.* **7** (2012), p. 699-712.
[6] D. Xiao, W. Yao, Q. Niu, "Valley-contrasting physics in graphene: magnetic moment and topological transport", *Phys. Rev. Lett.* **99** (2007), article no. 236809.
[7] W. Yao, D. Xiao, Q. Niu, "Valley-dependent optoelectronics from inversion symmetry breaking", *Phys. Rev. B* **77** (2008), article no. 235406.
[8] D. Xiao, G.-B. Liu, W. Feng, X. Xu, W. Yao, "Coupled spin and valley physics in monolayers of MoS_2 and other group-VI dichalcogenides", *Phys. Rev. Lett.* **108** (2012), article no. 196802.
[9] H. Zeng, J. Dai, W. Yao, D. Xiao, X. Cui, "Valley polarization in MoS_2 monolayers by optical pumping", *Nat. Nanotechnol.* **7** (2012), p. 490-493.
[10] K. F. Mak, K. He, J. Shan, T. F. Heinz, "Control of valley polarization in monolayer MoS_2 by optical helicity", *Nat. Nanotechnol.* **7** (2012), p. 494-498.
[11] T. Cao, G. Wang, W. Han, H. Ye, C. Zhu, J. Shi, Q. Niu, P. Tan, E. Wang, B. Liu *et al.*, "Valley-selective circular dichroism of monolayer molybdenum disulphide", *Nat. Commun.* **3** (2012), article no. 887.
[12] H. Yu, X. Cui, X. Xu, W. Yao, "Valley excitons in two-dimensional semiconductors", *Nat. Sci. Rev.* **2** (2015), p. 57-70.
[13] D. Y. Qiu, H. Felipe, S. G. Louie, "Optical spectrum of MoS_2: many-body effects and diversity of exciton states", *Phys. Rev. Lett.* **111** (2013), article no. 216805.
[14] T. Korn, S. Heydrich, M. Hirmer, J. Schmutzler, C. Schüller, "Low-temperature photocarrier dynamics in monolayer MoS_2", *Appl. Phys. Lett.* **99** (2011), article no. 102109.
[15] A. M. Jones, H. Yu, N. J. Ghimire, S. Wu, G. Aivazian, J. S. Ross, B. Zhao, J. Yan, D. G. Mandrus, D. Xiao *et al.*, "Optical generation of excitonic valley coherence in monolayer WSe_2", *Nat. Nanotechnol.* **8** (2013), p. 634-638.

[16] G. Moody, C. K. Dass, K. Hao, C.-H. Chen, L.-J. Li, A. Singh, K. Tran, G. Clark, X. Xu, G. Berghäuser *et al.*, "Intrinsic homogeneous linewidth and broadening mechanisms of excitons in monolayer transition metal dichalcogenides", *Nat. Commun.* **6** (2015), article no. 8315.

[17] H. Fang, C. Battaglia, C. Carraro, S. Nemsak, B. Ozdol, J. S. Kang, H. A. Bechtel, S. B. Desai, F. Kronast, A. A. Unal *et al.*, "Strong interlayer coupling in van der Waals heterostructures built from single-layer chalcogenides", *Proc. Natl Acad. Sci. USA* **111** (2014), p. 6198-6202.

[18] X. Hong, J. Kim, S.-F. Shi, Y. Zhang, C. Jin, Y. Sun, S. Tongay, J. Wu, Y. Zhang, F. Wang, "Ultrafast charge transfer in atomically thin MoS_2/WS_2 heterostructures", *Nat. Nanotechnol.* **9** (2014), p. 682-686.

[19] C.-H. Lee, G.-H. Lee, A. M. Van Der Zande, W. Chen, Y. Li, M. Han, X. Cui, G. Arefe, C. Nuckolls, T. F. Heinz *et al.*, "Atomically thin p–n junctions with van der Waals heterointerfaces", *Nat. Nanotechnol.* **9** (2014), p. 676-681.

[20] P. Rivera, J. R. Schaibley, A. M. Jones, J. S. Ross, S. Wu, G. Aivazian, P. Klement, K. Seyler, G. Clark, N. J. Ghimire *et al.*, "Observation of long-lived interlayer excitons in monolayer $MoSe_2$–WSe_2 heterostructures", *Nat. Commun.* **6** (2015), article no. 6242.

[21] H. Yu, Y. Wang, Q. Tong, X. Xu, W. Yao, "Anomalous light cones and valley optical selection rules of interlayer excitons in twisted heterobilayers", *Phys. Rev. Lett.* **115** (2015), article no. 187002.

[22] P. Rivera, K. L. Seyler, H. Yu, J. R. Schaibley, J. Yan, D. G. Mandrus, W. Yao, X. Xu, "Valley-polarized exciton dynamics in a 2D semiconductor heterostructure", *Science* **351** (2016), p. 688-691.

[23] K. L. Seyler, P. Rivera, H. Yu, N. P. Wilson, E. L. Ray, D. G. Mandrus, J. Yan, W. Yao, X. Xu, "Signatures of moiré-trapped valley excitons in $MoSe_2$/WSe_2 heterobilayers", *Nature* **567** (2019), p. 66-70.

[24] K. Tran, G. Moody, F. Wu, X. Lu, J. Choi, K. Kim, A. Rai, D. A. Sanchez, J. Quan, A. Singh *et al.*, "Evidence for moiré excitons in van der Waals heterostructures", *Nature* **567** (2019), no. 7746, p. 71-75.

[25] C. Jin, E. C. Regan, A. Yan, M. I. B. Utama, D. Wang, S. Zhao, Y. Qin, S. Yang, Z. Zheng, S. Shi *et al.*, "Observation of moiré excitons in WSe_2/WS_2 heterostructure superlattices", *Nature* **567** (2019), no. 7746, p. 76-80.

[26] C. Jin, E. Y. Ma, O. Karni, E. C. Regan, F. Wang, T. F. Heinz, "Ultrafast dynamics in van der Waals heterostructures", *Nat. Nanotechnol.* **13** (2018), p. 994-1003.

[27] P. Rivera, H. Yu, K. L. Seyler, N. P. Wilson, W. Yao, X. Xu, "Interlayer valley excitons in heterobilayers of transition metal dichalcogenides", *Nat. Nanotechnol.* **13** (2018), p. 1004-1015.

[28] D. Unuchek, A. Ciarrocchi, A. Avsar, K. Watanabe, T. Taniguchi, A. Kis, "Room-temperature electrical control of exciton flux in a van der Waals heterostructure", *Nature* **560** (2018), p. 340-344.

[29] A. Ciarrocchi, D. Unuchek, A. Avsar, K. Watanabe, T. Taniguchi, A. Kis, "Polarization switching and electrical control of interlayer excitons in two-dimensional van der Waals heterostructures", *Nat. Photon.* **13** (2019), p. 131-136.

[30] E. M. Alexeev, D. A. Ruiz-Tijerina, M. Danovich, M. J. Hamer, D. J. Terry, P. K. Nayak, S. Ahn, S. Pak, J. Lee, J. I. Sohn *et al.*, "Resonantly hybridized excitons in moiré superlattices in van der Waals heterostructures", *Nature* **567** (2019), p. 81-86.

[31] H. Yu, G.-B. Liu, J. Tang, X. Xu, W. Yao, "Moiré excitons: From programmable quantum emitter arrays to spin-orbit–coupled artificial lattices", *Sci. Adv.* **3** (2017), article no. e1701696.

[32] Y. Wang, Z. Wang, W. Yao, G.-B. Liu, H. Yu, "Interlayer coupling in commensurate and incommensurate bilayer structures of transition-metal dichalcogenides", *Phys. Rev. B* **95** (2017), article no. 115429.

[33] C. Zhang, C.-P. Chuu, X. Ren, M.-Y. Li, L.-J. Li, C. Jin, M.-Y. Chou, C.-K. Shih, "Interlayer couplings, Moiré patterns, and 2D electronic superlattices in MoS_2/WSe_2 hetero-bilayers", *Sci. Adv.* **3** (2017), article no. e1601459.

[34] H. Yu, G.-B. Liu, W. Yao, "Brightened spin-triplet interlayer excitons and optical selection rules in van der Waals heterobilayers", *2D Mater.* **5** (2018), article no. 035021.

[35] F. Wu, T. Lovorn, A. MacDonald, "Theory of optical absorption by interlayer excitons in transition metal dichalcogenide heterobilayers", *Phys. Rev. B* **97** (2018), article no. 035306.

[36] X. Zou, Y. Liu, B. I. Yakobson, "Predicting dislocations and grain boundaries in two-dimensional metal-disulfides from the first principles", *Nano Lett.* **13** (2012), p. 253-258.

[37] A. M. Van Der Zande, P. Y. Huang, D. A. Chenet, T. C. Berkelbach, Y. You, G.-H. Lee, T. F. Heinz, D. R. Reichman, D. A. Muller, J. C. Hone, "Grains and grain boundaries in highly crystalline monolayer molybdenum disulphide", *Nat. Mater.* **12** (2013), p. 554-561.

[38] W. Zhou, X. Zou, S. Najmaei, Z. Liu, Y. Shi, J. Kong, J. Lou, P. M. Ajayan, B. I. Yakobson, J.-C. Idrobo, "Intrinsic structural defects in monolayer molybdenum disulfide", *Nano Lett.* **13** (2013), p. 2615-2622.

[39] D. Le, T. S. Rahman, "Joined edges in MoS_2: metallic and half-metallic wires", *J. Phys.: Condens. Matter* **25** (2013), article no. 312201.

[40] H. Liu, L. Jiao, F. Yang, Y. Cai, X. Wu, W. Ho, C. Gao, J. Jia, N. Wang, H. Fan *et al.*, "Dense network of one-dimensional midgap metallic modes in monolayer $MoSe_2$ and their spatial undulations", *Phys. Rev. Lett.* **113** (2014), article no. 066105.

[41] O. Lehtinen, H.-P. Komsa, A. Pulkin, M. B. Whitwick, M.-W. Chen, T. Lehnert, M. J. Mohn, O. V. Yazyev, A. Kis, U. Kaiser *et al.*, "Atomic scale microstructure and properties of Se-deficient two-dimensional $MoSe_2$", *ACS Nano* **9** (2015), p. 3274-3283.

[42] J. Lin, S. T. Pantelides, W. Zhou, "Vacancy-induced formation and growth of inversion domains in transition-metal dichalcogenide monolayer", *ACS Nano* **9** (2015), p. 5189-5197.

[43] Y.-C. Lin, T. Björkman, H.-P. Komsa, P.-Y. Teng, C.-H. Yeh, F.-S. Huang, K.-H. Lin, J. Jadczak, Y.-S. Huang, P.-W. Chiu *et al.*, "Three-fold rotational defects in two-dimensional transition metal dichalcogenides", *Nat. Commun.* **6** (2015), article no. 6736.

[44] S. Barja, S. Wickenburg, Z.-F. Liu, Y. Zhang, H. Ryu, M. M. Ugeda, Z. Hussain, Z.-X. Shen, S.-K. Mo, E. Wong *et al.*, "Charge density wave order in 1D mirror twin boundaries of single-layer $MoSe_2$", *Nat. Phys.* **12** (2016), p. 751-756.

[45] Y. Ma, S. Kolekar, H. Coy Diaz, J. Aprojanz, I. Miccoli, C. Tegenkamp, M. Batzill, "Metallic twin grain boundaries embedded in $MoSe_2$ monolayers grown by molecular beam epitaxy", *ACS Nano* **11** (2017), p. 5130-65139.

[46] H.-P. Komsa, A. V. Krasheninnikov, "Engineering the electronic properties of two-dimensional transition metal dichalcogenides by introducing mirror twin boundaries", *Adv. Electron. Mater.* **3** (2017), article no. 1600468.

[47] P. Moon, M. Koshino, "Electronic properties of graphene/hexagonal-boron-nitride moiré superlattice", *Phys. Rev. B* **90** (2014), article no. 155406.

[48] W. Yao, S. A. Yang, Q. Niu, "Edge states in graphene: From gapped flat-band to gapless chiral modes", *Phys. Rev. Lett.* **102** (2009), article no. 096801.